remote sensing

MDPI

Article

Extracting Mare-like Cryptomare Deposits in Cryptomare Regions Based on CE-2 MRM Data Using SVM Method

Tianqi Tang [1,2], Zhiguo Meng [1,2], Yi Lian [3], Zhaoran Wei [1], Xuegang Dong [1], Yongzhi Wang [1,2,*], Mingchang Wang [1], Zhanchuan Cai [2], Xiaoping Zhang [2], Alexander Gusev [4] and Yuanzhi Zhang [5,6]

1 College of Geoexploration Science and Technology, Jilin University, Changchun 130026, China
2 State Key Laboratory of Lunar and Planetary Sciences, Macau University of Science and Technology, Macau 999078, China
3 College of Geographic and Environmental Sciences, Tianjin Normal University, Tianjin 300387, China
4 Institute of Geology, Kazan Federal University, Kazan 420008, Russia
5 Key Laboratory of Lunar and Deep-Space Exploration, National Astronomical Observatories, Chinese Academy of Sciences, Beijing 100101, China
6 School of Astronomy and Space Science, University of Chinese Academy of Sciences, Beijing 100049, China
* Correspondence: wangyongzhi@jlu.edu.cn; Tel.: +86-186-4306-2191

Abstract: A new kind of surface material is found and defined in the Balmer–Kapteyn (B-K) cryptomare region, Mare-like cryptomare deposits (MCD), representing highland debris mixed by mare deposits with a certain fraction. This postulates the presence of surface materials in the cryptomare regions. In this study, to objectively verify the existence of the MCD in the cryptomare regions, based on the Chang'E-2 microwave radiometer (MRM) data, the support vector machine (SVM) method was adopted, where the K-means algorithm was used to optimize the training samples and the random forest algorithm was used to select the proper band features. Finally, the extracted MCD is identified with the datasets including Lunar Reconnaissance Orbiter Wide Angle Camera, Diviner, and Clementine UV–VIS. The main findings are as follows: (1) Compared to the range outlined via the TB counter, the range of the MCD is objectively extracted using the SVM method in the B-K cryptomare region, which is reasonably indicated by the FeO abundance, TiO_2 abundance, and rock abundance distributions. (2) The MCDs were extracted in the Dewar, Lomonosov–Fleming (L-F), and Schiller–Schickard (S-S) regions, indicating that the MCDs are widely distributed in the cryptomaria. (3) The presence of MCDs is concentrated in a limited region, accounting for 64.9%, 52.3%, 76.4%, and 64%, respectively, in the range of Dewar, L-F, S-S, and B-K regions identified using the optical data. The occurrence of the MCD gives a new understanding of the surface evolution in the cryptomare regions.

Keywords: mare-like cryptomare deposits; support vector machine; microwave radiometer data; K-means algorithm; random forest algorithm; cryptomare

Citation: Tang, T.; Meng, Z.; Lian, Y.; Wei, Z.; Dong, X.; Wang, Y.; Wang, M.; Cai, Z.; Zhang, X.; Gusev, A.; et al. Extracting Mare-like Cryptomare Deposits in Cryptomare Regions Based on CE-2 MRM Data Using SVM Method. *Remote Sens.* **2023**, *15*, 2010. https://doi.org/10.3390/rs15082010

Academic Editors: Giancarlo Bellucci and Christian Wöhler

Received: 19 January 2023
Revised: 14 March 2023
Accepted: 7 April 2023
Published: 11 April 2023

1. Introduction

Early in lunar history, ancient basalts existed extensively, a considerable portion of which have been destroyed or shaded by the impact events and their associated ejecta or have been buried by younger lunar basalts, forming the cryptomare [1,2]. The surface deposits in the cryptomare regions are difficult to detect by optical techniques, as the long-term impact of ejecta contamination and space weathering decreases the differences in the deposits from the beyond highlands [3,4]. Thus, the surface deposits in cryptomaria are a mysterious and usually invisible part of the lunar upper crust. Therefore, the study of the range and compositions of the surface deposits in cryptomare will provide important contributions to better understand the ancient volcanism and surface evolution of the Moon [3,5].

Currently, the presence of dark-haloed craters (DHCs) plays an important role in pursuing the range and compositions of cryptomaria [2,3,6–10]. The DHCs have a relatively symmetrical halo of dark materials surrounding an impact crater within a limited range [2], where the dark materials are basaltic deposits exhumed by cratering. Additionally, mixed spectral analysis is also used to evaluate the range and compositions of surface deposits in the cryptomaria [11–13]. Mustard et al. [12] used a Galileo solid-state imaging (SSI) instrument to confirm the strong mafic affinities of the DHCs and the enhanced mafic content of the light plains within the cryptomaria. Additionally, Head et al. [13] showed local mafic enhancements in the distal Hevelius Formation and associated deposits, the largest of which are interpreted to represent the presence of pre-Orientale mare deposits in the Mendel–Rydberg (M-R) cryptomare. Hawke et al. [14] and Giguere et al. [10] also found the mafic anomalies in Lomonosov–Fleming (L-F) cryptomare using remote sensing data and Clementine multispectral data. Using Chandrayaan-1 Moon Mineralogy Mapper (M^3) hyperspectral data, Whitten and Head [3] proposed that the mafic increases are widely distributed in the Balmer–Kapteyn (B-K), L-F, Schiller–Schickard (S-S), and M-R cryptomare regions. This finding is also supported by Hawke et al. [9] using the Lunar Prospector (LP) gamma-ray spectrometer (GRS) data, and Lawrence et al. [15] identified a new cryptomare in the Dewar region using the same dataset. Besides the enhanced mafic content, Wang and Qiu [4] and Qiu et al. [16] discovered ferroan anorthosite suite and magnesian suite in the southern part of the B-K region based on Chang'E(CE)-1 interference imaging spectrometer (IIM) hyperspectral data. Limited by the penetration depth and space weathering, the study using the optical data differs greatly from each other in surface deposits and their distributions.

In China's Chang'E (CE)-1/2 missions, a microwave radiometer (MRM) onboard the satellite passively measured the brightness temperature (TB) of the regolith. The penetration depths of the MRM data can be up to several meters below the surface [17] and the data are sensitive to the surface deposits of the geologic units on the Moon as shown in Figure 1 [18,19]. Moreover, as mentioned above, the mafic increases are widely distributed in the cryptomare regions, and the increase in the mafic deposits will apparently impact the propagation of the microwave. Thus, the MRM data will be able to give a new view of the surface deposits in the cryptomaria. Using the CE-2 MRM data, for the first time, Tang et al. [20] discovered and identified a new material with extensive distribution in the B-K cryptomare region, named the mare-like cryptomare deposit (MCD), which is the highland debris mixed by mare deposits with a certain fraction. Using ground-based (AO and GBO) and monostatic orbital (Lunar Reconnaissance Orbiter Miniature Radio Frequency Instrument, LRO Mini-RF) radar data, Bramson et al. [5] found the characteristic low backscatter in the S-S region, which is likely brought by the attenuating nature in radio waves of some basaltic minerals. This partly supports the reasonability of the MCDs in the cryptomaria, which is of great significance in studying the surface deposits of the cryptomare regions. Whereas, Tang et al. [20] largely outlined the range of the MCD according to the specified TB contour. Moreover, whether the MCD exists in all cryptomare regions or not should be systematically studied. Therefore, to further understand the existence of the MCD and its geologic significance, a new method is indispensable to objectively extract the MCD in the cryptomaria.

Recently, the support vector machine (SVM) method has been widely used in lunar remote sensing [21,22]. SVM is a method to separate classes of interest [21] and usually produces higher classification accuracy compared to the traditional methods, e.g., the maximum likelihood method [23]. Kodikara et al. [21] used the SVM algorithm to classify lunar regolith types, particle size, maturity, and the dominant type of pyroxene. Chen et al. [22] proposed that the salient region of impact craters could be correctly detected by using the SVM method using the lunar image data from CE-1 and CE-2 satellites. Qiu et al. [16] estimated the abundances and distributions of chemical components in the B-K region using the same method. Because of the advantage of treating the heterogeneity deposits

with limited training samples [23], the SVM method is an appealing candidate to extract the MCD.

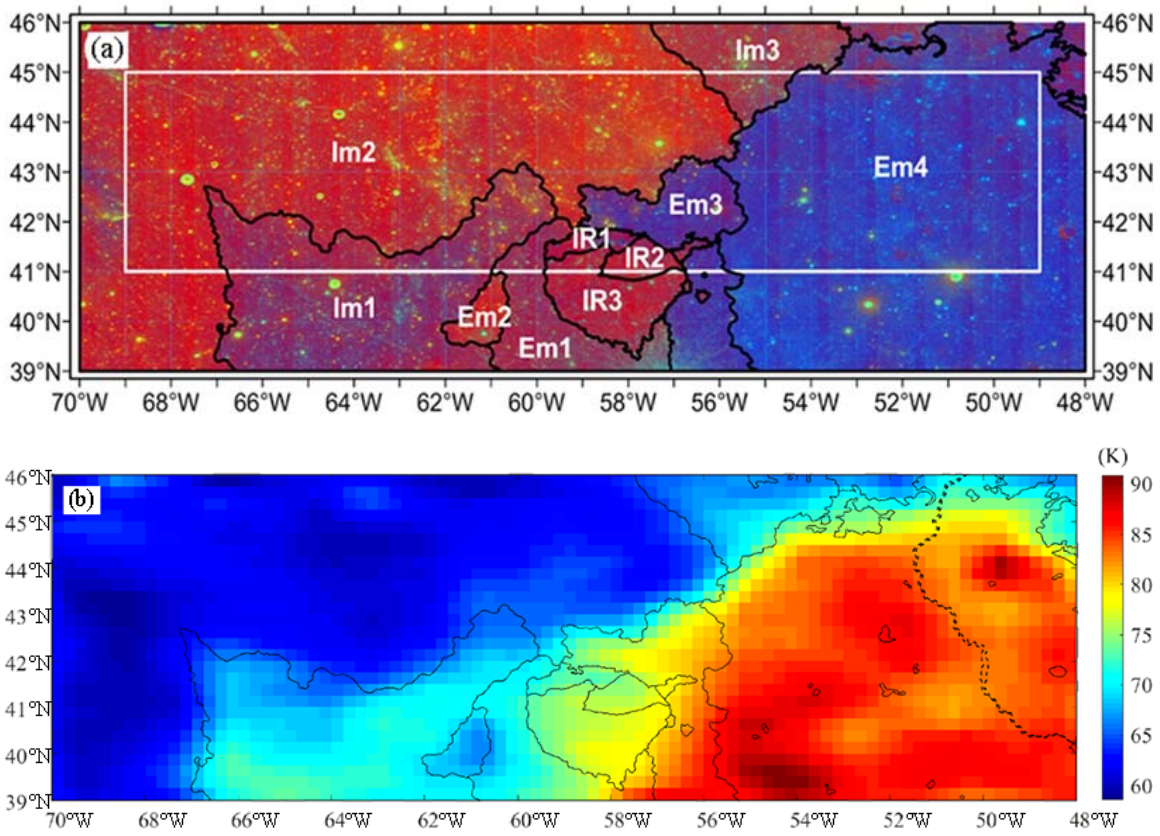

Figure 1. (**a**) The map of geological interpretation of Chang 'E-5 landing area interpreted by Qian et al. [24]. (**b**) 37-GHz brightness temperature difference map [19], where the black line is the geological units interpreted by Qian et al. [24].

In this paper, the SVM method is employed to extract the MCD in the cryptomare regions. The processing of the CE-2 MRM data is presented in Section 2. Then, the way to extract the MCD with the SVM method is described in Section 3. Here, the K-means algorithm is used to optimize the training samples, and the random forest algorithm is used to select the proper bands. Section 4 provides and discusses the results of the extracted MCDs in Dewar, L-F, S-S, and B-K cryptomaria. Section 5 is the conclusions.

2. Data Processing

2.1. Study Regions and Regional Geology

Buried mare deposits were first designated as cryptomare by Head and Wilson [1]. Using Chandrayaan-1 M^3 hyperspectral data; Whitten and Head [3] determined the typical cryptomaria on the Moon, including Dewar, L-F, S-S, and B-K (Figure 2).

The Dewar crater (2.66°S, 165.60°E), located in the highlands northwest of the South Pole-Aiken Basin (49.37°S, 157.95E), is an Imbrian-aged impact structure with a 50 km diameter. No mare basalt ponds have been identified in the region to date using optical data. Lawrence et al. found four DHCs surrounding the Dewar crater [25]. After excluding the existence of a deposit of mafic impact melt or mare basalts or pyroclastics, Lawrence et al. [25] proposed that the region is a cryptomare.

L-F is primarily centered on the pre-Nectarian Lomonosov–Fleming Basin (19°N, 105°E) on the east side of the Moon, located east and northeast of Mare Marginis. Seventeen well-developed DHCs were mapped by Giguere et al. [10], indicating the presence of cryptomare. The mafic geochemical anomaly has been widely studied by using Apollo

orbital geochemistry data [14,26–28], Lunar Prospector data sets [29], and Clementine multispectral images [10].

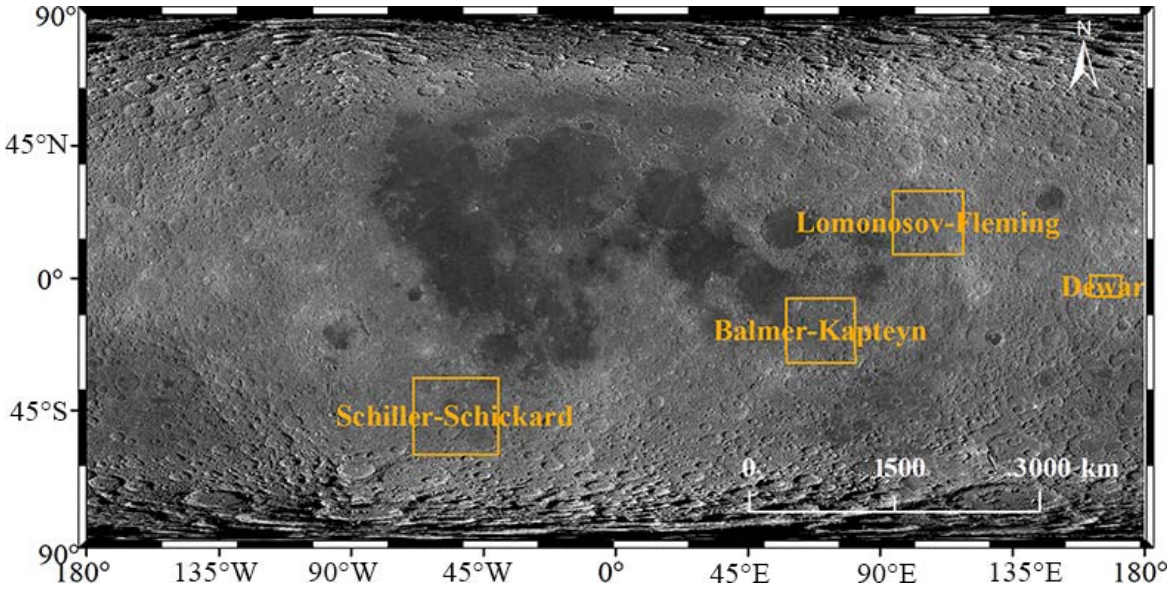

Figure 2. Wide angle camera (WAC) image of study regions: the wide angle camera data (100 m/pixel) of the Lunar Reconnaissance Orbiter Camera (LROC) system. The orange rectangles indicate the positions of the Dewar, Lomonosov–Fleming, Schiller–Schickard, and Balmer–Kapteyn cryptomare regions on the Moon, respectively.

The S-S region is formed in the pre-Orientale, located southwest of the far side of the Moon, including light plain deposits, dark-haloed craters, and mare units. Twelve DHCs were delineated by Blewett et al. [30] and distributed on the surface of the region. The surface deposits of the S–S cryptomare region have been studied well by utilizing a combination of spectral mixing analyses [13,30–32], DHCs and geochemical anomalies [3,7,14,33], and radar signatures [5,34].

The pre-Nectarian B-K region is located east of Mare Fecunditatis on the east limb of the Moon, southwest of Mare Smythii. There exist several large craters including Langrenus, Petavius, Kapteyn, and La Pérouse craters and a wide range of light plain deposits on the surface [9]. Hawke et al. [9] identified 25 DHCs in the region, covering an area of up to 60,600 km^2. The surface deposits in the B-K region have been comprehensively studied with multiple spacecraft images, including Lunar Orbiter data, Clementine multispectral data, and LP-GRS data [1,8].

2.2. Microwave Radiometer Data

The MRM data used are from the CE-2 satellite, which orbited the Moon at an altitude of 100 km from October 2010 to June 2011 [17,35]. Table 1 shows the main parameters of CE-2 MRM. The MRM instrument works at four frequencies of 3.0 GHz, 7.8 GHz, 19.35 GHz, and 37 GHz, and the spatial resolution of each frequency is about 25 km (about 1°) at 3.0 GHz, 17.5 km at 7.8 GHz, 17.5 km at 19.35 GHz, and 17.5 km at 37 GHz, respectively [18,34]. The observation angle of the instrument is 0°, and the radiation sensitivity of MRM data is better than 0.5 K [17]. The MRM data are at the 2C level, which is after geometric correction and radiometric calibration [17,35,36]. Data are stored in PDS format, including observation time, four-channel brightness temperature values, solar azimuth and incident angle, longitude, latitude, orbital height, and data quality.

Table 1. Main parameters of Chang'E-2 microwave radiometer.

Frequency (GHz)	3.0	7.8	19.35	37
Bandwidth (MHz)	100	200	500	500
Integration time (ms)	200	200	200	200
Temperature sensitivity (K)	≤0.5	≤0.5	≤0.5	≤0.5
3 dB beam width	E: 15 + 2°	E: 9 + 2°	E: 9 + 2°	E: 10 + 2°
	H: 12 + 2°	H: 9 + 2°	H: 10 + 2°	H: 10 + 2°

The MRM data can reflect the thermal emission features of the lunar regolith at different depths, which are related to the used wavelengths [34,37]. The data have been shown to be sensitive to the dielectric properties of the substrate deposits [36,38], which are less impacted by ejecta contamination and space weathering [17,39,40]. Therefore, the CE-2 MRM data provide a potential opportunity to evaluate the surface deposits in cryptomare regions.

2.3. TB Maps Generation

The generation of the brightness temperature (TB) maps has been described in detail by Chan et al. [41], Cai and Lan [35], Meng et al. [18], and Tang et al. [20]. The brightness temperature changes greatly with time, which is not advantageous to evaluate the dielectric properties of the regolith over the Moon [20]. In order to accurately express the spatial variation of the TB, the hour angle was introduced to represent the passing time of the MRM data points on the Moon [42]. Thus, MRM data points were divided into 24 intervals corresponding to 24 h in a lunation; 1366, 6589, 9327, and 6508 MRM data points are selected, respectively, based on the ranges of Dewar, L-F, S-S, and B-K regions, and the selected data are then ascribed into 24 h angles. After comparison, the data points from 14:00 to 15:00 and 4:00 to 5:00 are used to map the Dewar region, representing the TB during the daytime and night. Similarly, data points from 13:00 to 14:00 and 22:00 to 23:00 are selected for the L-F region; data points from 14:00 to 15:00 and from 05:00 to 06:00 are selected for the S-S region and data points from 11:00 to 12:00 and 22:00 to 23:00 are selected for the B-K region. Thereafter, the linear interpolation method is used to make the TB maps with a spatial resolution of 0.25° × 0.25°, about 7.5 km along the equator (Figure 3) [43].

Figure 3 shows that the interpolated maps accurately represent the selected MRM data. However, the variation of TB along the latitude is much larger than that brought by the regolith compositions indicated by values at the same latitude [39]. Here, the following two methods were adopted to weaken the change of the TB with latitude and to enhance the TB performances of the surface deposits.

The first method is the normalized TB (nTB) mapping, which was proposed by Meng et al. [18,39] to enhance the relationship between the TB and the surface deposits. To obtain the nTB maps, the standard TB values of every latitude were calculated according to the procedures provided in the references [18,39]. The nTB maps at daytime and night were generated by dividing the TB of every pixel by the standard TB of the corresponding latitude (Figure 4, Columns 1 and 2). The resulting nTB maps are considered to be sensitive to the compositions and thermal state of the surface deposits in the penetration depth [18,39].

The second method is the TB difference (dTB) mapping. The dTB is the difference between the interpolated daytime and night TB of the same frequency before normalization (Figure 4, Column 3). The dTB maps are a good reflection of the compositions of the surface deposits in the penetration depth [18,39].

To better understand the existences of the MCDs, the cryptomare regions in Dewar, L-F, S-S, and B-K cryptomare regions drawn by Whitten and Head [3] were vectorized and overlaid on generated nTB and dTB maps (Figure 4). The reasonability of the generated TB maps has been verified in the B-K region having good consistency [20].

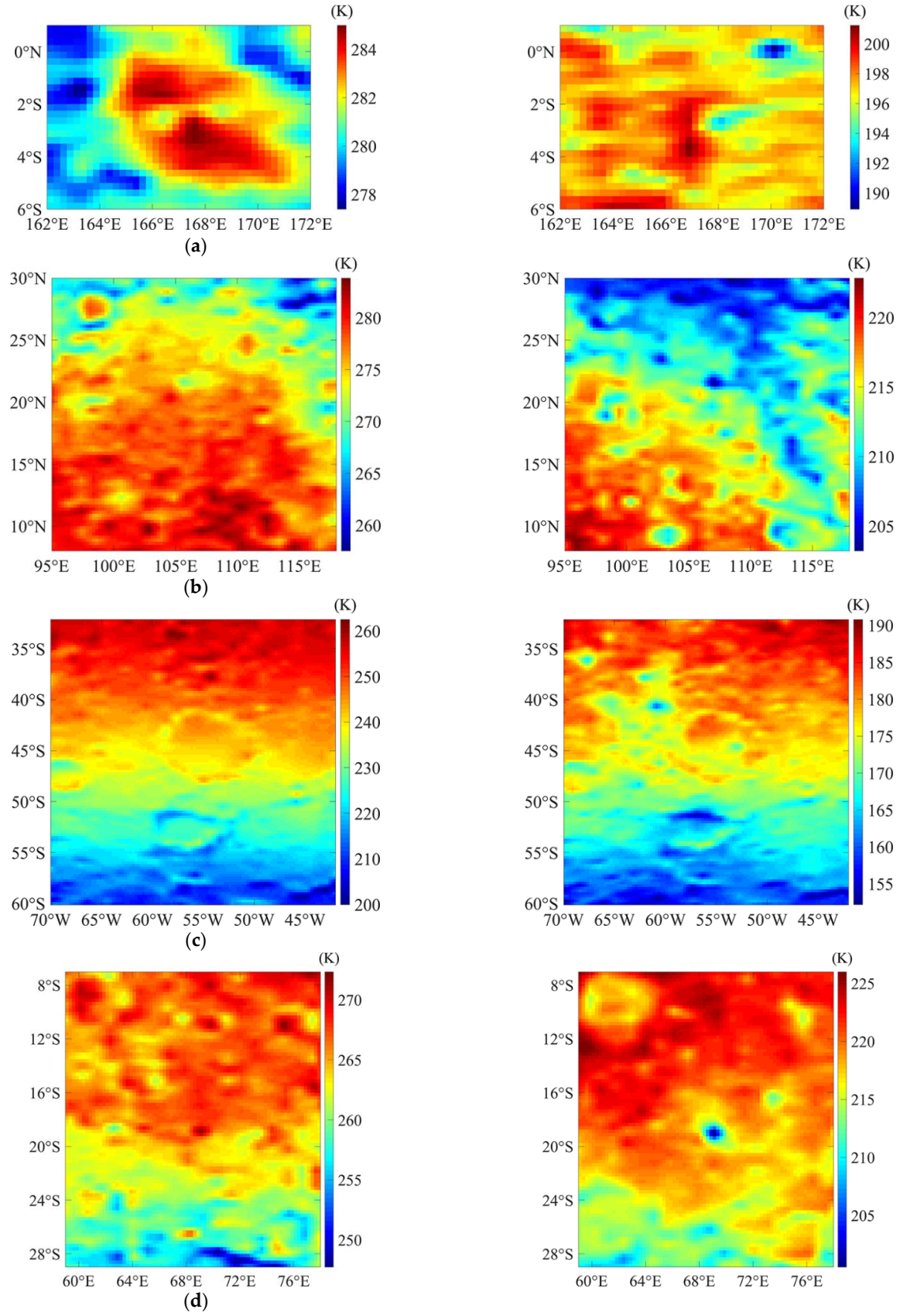

Figure 3. The brightness temperature maps at 37 GHz of the (**a**) Dewar, (**b**) Lomonosov–Fleming, (**c**) Schiller–Schickard, and (**d**) Balmer–Kapteyn cryptomare regions. Column 1 and Column 2 are the corresponding generated TB maps at daytime and night, respectively.

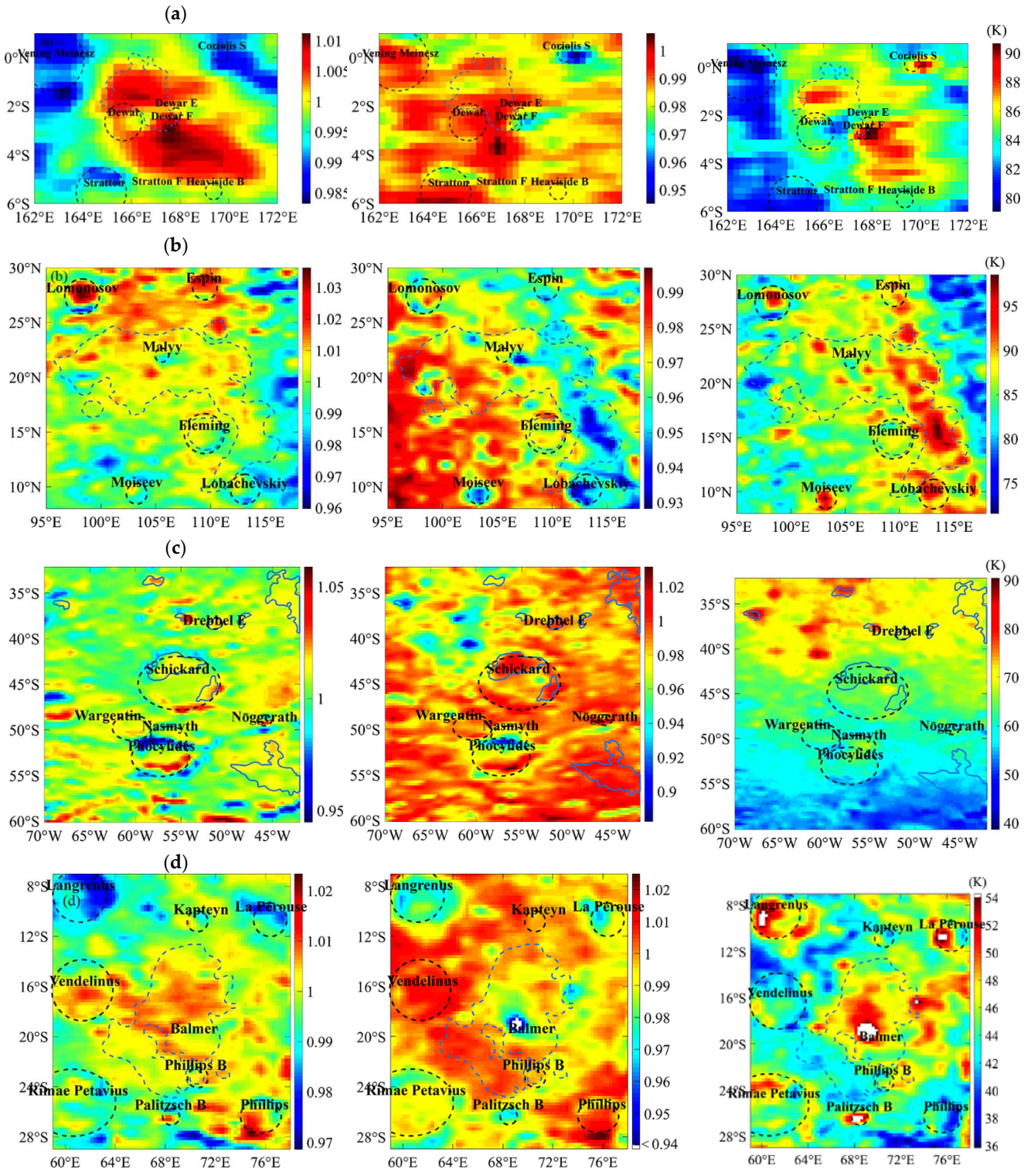

Figure 4. The nTB and dTB maps at 37 GHz of the (**a**) Dewar, (**b**) Lomonosov–Fleming, (**c**) Schiller–Schickard, and (**d**) Balmer–Kapteyn cryptomare regions. Column 1: nTB maps in daytime. Column 2: nTB maps at night. Column 3: dTB maps. The blue lines represent the cryptomare extents interpreted by Whitten and Head [3]. The black dotted lines represent the craters.

3. Methods

3.1. The Support Vector Machine Method

Support vector machine (SVM) is a machine learning algorithm suitable for sample learning with a small quantity, which generally produces a higher classification accuracy than traditional methods [23]. In a two-class pattern recognition problem where classes are linearly separable, the SVMs select the one linear decision boundary that leaves the greatest margin between the two classes. The margin is defined as the sum of the distances to the hyperplane from the closest points of the two classes. SVMs were initially designed for binary (two-class) problems. Therefore, the SVM algorithm was adopted to extract the MCD in cryptomare regions.

An SVM classifier performs binary classification, it separates a set of training vectors into two different classes. The training sample sets can be expressed as follows [21],

$$D = \{(x_1, y_1), (x_2, y_2), \cdots, (x_M, y_M)\}, y_i \in \{-1, +1\}$$

where M is the number of the training samples; $x_i = \{nTB_{i1}, nTB_{i2}, \cdots, dTB_{iT}\}$, T is the number of the band features, and y_i is the membership labels to distinguish the MCD associated with each vector x_i.

Generally, according to the selected training samples, two classes are linearly separable. This means that it is possible to find at least one hyperplane defined by a vector and a bias that can separate the two classes without errors. The membership decision rule can be based on the discriminant function associated with the hyperplane. The function is defined as,

$$y_i = \boldsymbol{\omega}^T \boldsymbol{x} + b \tag{1}$$

where $\boldsymbol{\omega}$ and b are model parameters. In order to find such a hyperplane, the SVM approach consists of finding the optimal hyperplane that maximizes the distance between the closest training sample and the separating hyperplane. The distance can be expressed as:

$$r = \frac{|\boldsymbol{\omega}^T \boldsymbol{x} + b|}{\|\boldsymbol{\omega}\|} \tag{2}$$

To classify the training samples into the correct categories, the following expression should be provided.

$$\begin{cases} \boldsymbol{\omega}^T \boldsymbol{x}_i + b \geq +1, & y_i = +1 \\ \boldsymbol{\omega}^T \boldsymbol{x}_i + b \leq -1, & y_i = -1 \end{cases} \tag{3}$$

The geometrical margin between the two classes can be expressed as the following,

$$\gamma = \frac{2}{\|\boldsymbol{\omega}\|} \tag{4}$$

where γ is called the margin.

To find the hyperplane with the maximum margin, that is, to find the parameters $\boldsymbol{\omega}$ and b that can satisfy the constraints in Formula (3), so that γ is the maximum:

$$\begin{aligned} &\underset{\omega,b}{max} \tfrac{2}{\|\boldsymbol{\omega}\|} \\ &y_i\left(\boldsymbol{\omega}^T \boldsymbol{x}_i + b\right) \geq 1,\ i = 1, 2, \cdots n \end{aligned} \tag{5}$$

Obviously, in order to maximize the margin, we only need to maximize $\|\boldsymbol{\omega}\|^{-1}$ which is equivalent to minimizing $\|\boldsymbol{\omega}\|^2$, so we can rewrite Formula (5) as Formula (6). Consequently, it turns out that the optimal hyperplane can be determined to identify the MCD as the solution of the following convex quadratic programming problem:

$$\begin{aligned} &\min_{\omega,b} \tfrac{1}{2}\|\boldsymbol{\omega}\|^2 \\ &y_i\left(\boldsymbol{\omega}^T \boldsymbol{x}_i + b\right) \geq 1,\ i = 1, 2, \cdots n \end{aligned} \tag{6}$$

In this study, the TB features can be used including the four-band nTB at daytime, four-band nTB at night, and four-band dTB maps; that is, the number of the band features

is 12. To obtain the classification with good precision, the training samples should be optimized, and the band features should be refined before operating the SVM method.

3.2. Training Samples Optimization

Tang et al. [20] first proposed the existence of the MCD, but the materials with low-dTB anomaly and the materials without a clear category also exist in the range of the cryptomare interpreted by Whitten and Head [3]. Therefore, when selecting the TB within the range of cryptomare, the first step should be to optimize the training samples to ensure the purity and representability of the training samples representing the MCD.

In this study, the K-means algorithm was adopted to optimize the training samples. This algorithm is characterized by fast computation speed and good clustering performance and has been widely applied in lunar research [44]. It is expected that the sample points within each class have high similarity, while the sample points between each class have a low similarity. According to the clustering performance index minimization principle, the clustering criterion function is the minimum sum of the squares of errors from each sample point within the class to the center of the class [45]. By selecting the training samples proportionally from the clustered categories, the K-means method can eliminate abnormally training samples that are far away from the clustering centers, and then optimize the training samples.

3.3. Extraction of Band Features

Random Forest (RF) is used to extract the band features appropriate for the identification of the MCD by identifying key features of the TB for machine learning while avoiding over-fitting of the model [46]. This algorithm has been introduced into related studies such as lunar crater detection and lunar module soft landing [47,48]. The RF implementations can provide measures of feature importance, and the important parameters are useful in the extraction of the proper band features to operate the SVM algorithm.

Training samples optimization can improve the sample homogeneity to optimize the accuracy of the calculated feature importance with the RF algorithm. The collected explanatory variables such as the TB features were subjected to an RF model based on the importance analysis of each variable by calculating the out-of-bag permuted predictor delta error, as expressed by

$$Vector\_IP(u_i) = \sum_{n=1}^{N} (errOOB\_noise_{ni} - errOOB_{ni})/N \quad (7)$$

where *Vector_IP* (u_i) is the importance of variable i to the model; N is the total number of decision trees, whose value is given as 200; n signifies the nth decision tree; $errOOB_{ni}$ is the out-of-bag data error, $errOOB\_noise_{ni}$ is the out-of-bag data error after adding random permutation, that is, $errOOB_{ni}$ and $errOOB\_noise_{ni}$ represent the out-of-bag errors of each decision tree before and after the random permutation of variable i.

Thus, with the optimized training samples and the extracted band features, based on Formulas (1)–(6), every pixel can be classified into a category, the MCD or not.

4. Results and Discussions

4.1. Extracting the MCD in Balmer–Kapteyn Cryptomare Region

Tang et al. [20] proposed the existence of the MCD, materials with low-dTB anomaly, and materials without a clear category in the B-K cryptomare region. That is, the categories of the surface deposits are k is set as 3. The optimization of the training samples are shown in Figure 5a, where the purple, blue, and yellow colors, respectively, represent low-dTB materials (category 1), materials not clearly categorized (category 2), and the MCD (category 3). Here, category 1 shows a distinctly different TB performance compared to category 3; meanwhile, the TB behaviors of category 2 are not clearly different from category 3. Therefore, category 1 was taken as non-MCD samples, while category 2 and category 3 were integrated as the MCD samples, which were then randomly sampled in a

20% proportion. Finally, 500 training samples in the B-K cryptomare region were selected. Such training samples optimization method can not only effectively avoid the output of a small sample clustering region but can also maximize the accuracy of classification.

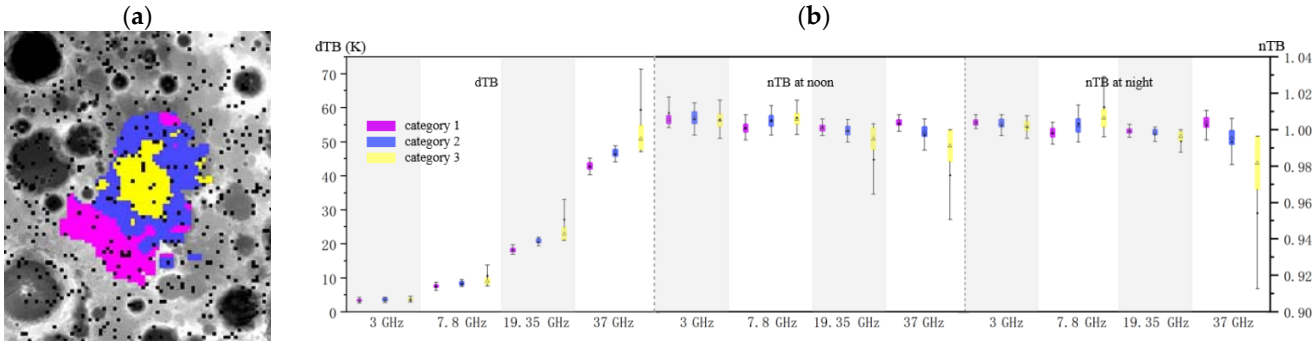

Figure 5. (**a**) The optimized training samples in the Balmer–Kapteyn cryptomare region. The purple, blue, and yellow colors respectively represent low-dTB material (category 1), materials without a clear category (category 2), and the MCD (category 3), overlayed on the DEM map. The black points are randomly sampled in a 20% proportion. (**b**) Numerical statistics of nTB and dTB characteristics of three categories.

Numerical statistics were conducted on the distribution characteristics of nTB and dTB of the optimized training samples, and the results showed that there were differences in the TB characteristics of the three categories as shown in Figure 5b. The median dTB values of the three categories were similar at 3.0 GHz and 7.8 GHz, about 3 K. However, the median dTB values of category 3 at 19.35 GHz and 37 GHz were higher than that of the other two categories by about 5 K and 12 K, respectively. The average dTB values of category 3 at 19.35 GHz and 37 GHz were higher than that of categories 1 and 2, by about 17 K and 13 K, respectively. As the frequency increases, the quartile difference between category 3 and categories 1 and 2 becomes larger, with the three categories having quartiles of 44 K, 48 K, and 54 K, respectively, at 37 GHz. In the dynamic ranges of dTB values, category 3 is obviously different from the others except at 3.0 GHz. From the upper limit and lower limit of nTB values, the nTB dynamic range of category 3 increases significantly with frequency increases. Therefore, the numerical statistics of TB values indicate that the training samples are well-optimized, which can better represent the corresponding category.

Using the RF algorithm, the importance of the band features can be calculated, as shown in Figure 6. Figure 6 shows that the feature importance is lowest at 7.8 GHz at night, followed by 7.8 GHz dTB, while it is highest at 37 GHz at noon, followed by 3.0 GHz dTB. To better represent the MCD, the band features with the top 6 importance are extracted to operate the SVM method. Because the surface deposits and the observation time are different from the four cryptomaria, the calculated feature importance is different. Therefore, the extracted band features for every cryptomare are shown in Table 2.

Table 2. The extracted band features of the Dewar, Lomonosov–Fleming, Schiller–Schickard, and Balmer–Kapteyn cryptomare regions.

Region	nTB at Noon	nTB at Night	dTB
Dewar	3.0, 19.35 GHz	3.0, 7.8 GHz, 19.35 GHz	37 GHz
L-F	37 GHz	3.0, 37 GHz	3.0, 19.35, 37 GHz
S-S	19.35 GHz	3.0, 19.35, 37 GHz	3.0, 37 GHz
B-K	37 GHz	3.0, 37 GHz	3.0, 19.35, 37 GHz

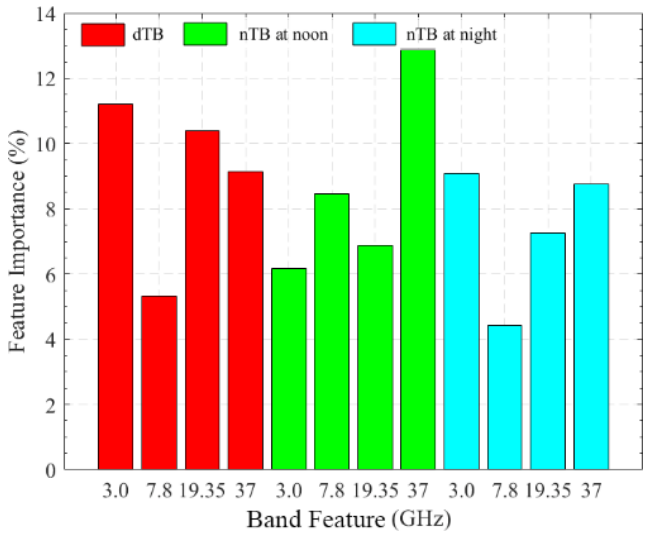

Figure 6. Importance of band features of nTB and dTB in the Balmer–Kapteyn cryptomare region.

Then, after optimizing the training samples and extracting the important band features, the MCD in the cryptomare region is classified by using the SVM method, as shown in Figure 7.

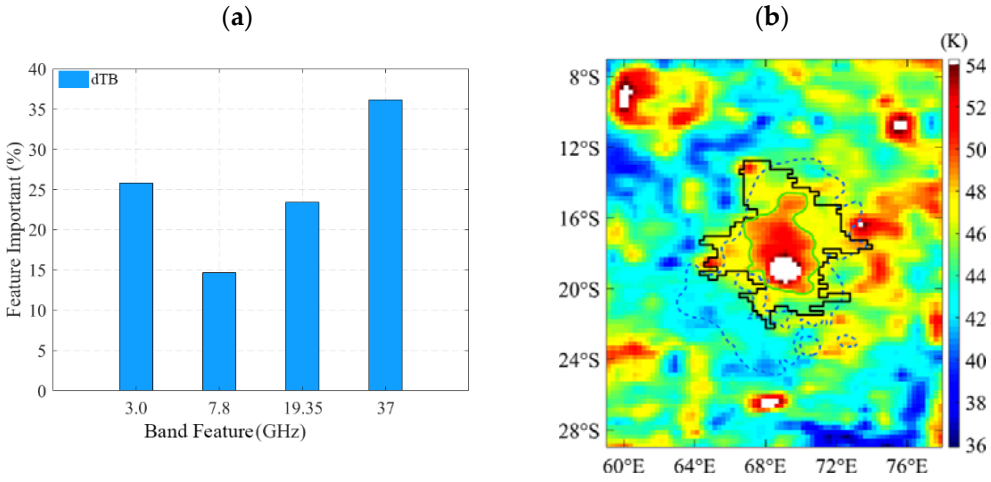

Figure 7. (**a**) Importance of four-band dTB features in the Balmer–Kapteyn cryptomare region. (**b**) The distribution of the extracted MCD (black line) in Balmer–Kapteyn cryptomare region. The extent of Balmer–Kapteyn cryptomare region interpreted by Whitten and Head [3] is outlined by the blue dotted line [3]. The MCD region presented by Tang et al. [20] is indicated by the green line.

Moreover, previous studies appreciate the dTB maps in analyzing the surface deposits [39,43]. Thus, to better understand the relationship between the TB map and the surface deposits, the RF algorithm is used to extract the proper dTB map as the background to postulate the distribution of the retrieved MCD, as shown in Figure 7a. To evaluate the reasonability of the new range of the region with MCD, the extent of the cryptomare region interpreted by Whitten and Head [3], and the MCD range presented by Tang et al. [20] are vectorized and overlaid on the extracted dTB map with the blue dotted line and green line, respectively (Figure 7b).

Figure 7 presents that the extracted MCD with the SVM method is reasonable, which is indicated by the following four aspects.

First, the range of the extracted MCD is reasonable. Here, the MCD is first presented by Tang et al. [20] (named Tang-MCD), while the range was indicated by using the 48-K-dTB isotherm. Whereas, Figures 4 and 7 indicate that the TB behaviors within the range of

Tang-MCD are similar to the nearby region. In this study, the MCD extracted with the SVM method almost covers the whole area with similar TB behaviors compared to Tang-MCD. Comparatively speaking, the new range is more objective and the range is more reasonable than before. The new range extends towards the north, northeast and west of the B-K region, about 24,802.4 km^2, which is about 63% larger than that of the Tang-MCD.

Second, the range of the extracted MCD agrees well with the cryptomare range provided by Whitten and Head [3] in the northwest, east and southeast boundaries. Even in the southwest boundary, the two ranges indicate a big difference, but they are similar in pattern.

Third, the wide-angle camera (WAC) image, FeO abundance (FA), TiO_2 abundance (TA), and rock abundance (RA) were adopted to verify the existence of the MCD (Figure 8). Here, the WAC data are downloaded from the wide-angle camera data (100 m/pixel) of the Lunar Reconnaissance Orbiter Camera (LROC) system; the FA and TA data are derived with the improved Lucey model [47] using the Clementine UV-VIS data, and the RA data are recorded by Diviner instrument on LRO satellite and the method developed by Bandfield et al. [48]. The average FA, TA, and RA with the range of the MCD (named Region MCD) and beyond (named Region N) are counted, as shown in Table 3.

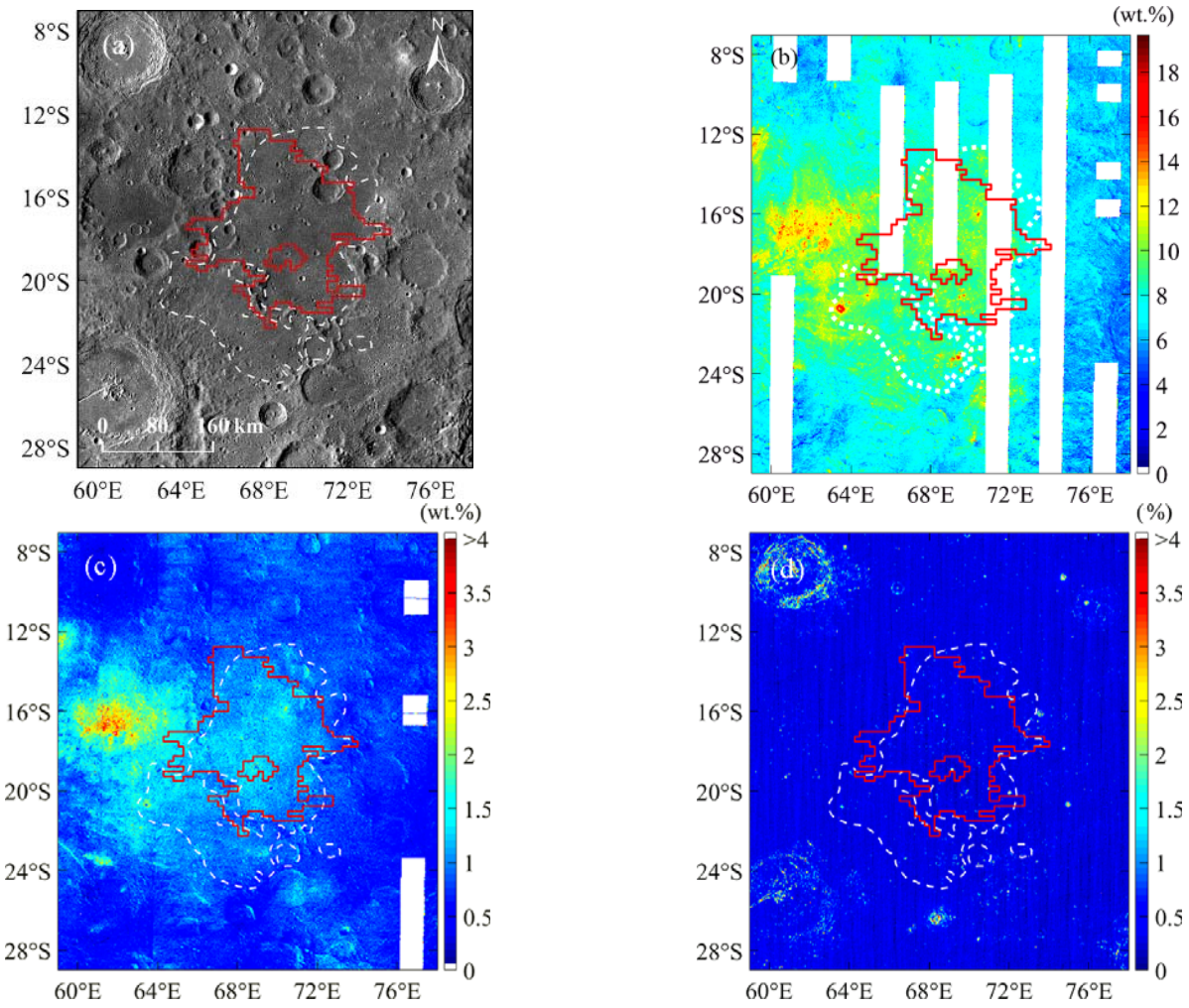

Figure 8. The maps in the Balmer–Kapteyn cryptomare region. (**a**) WAC image map; (**b**) FeO abundance map; (**c**) TiO_2 abundance map; (**d**) Rock abundance map. The red line is the MCD extracted in this study. The white dotted line is the cryptomare region interpreted by Whitten and Head [3].

Table 3. The FeO abundance, TiO_2 abundance, and rock abundance of Region MCD (MCD) and Region N (N) in the Balmer–Kapteyn cryptomare region.

Compositions	Abundance	
	MCD	N
FA	9.67 wt.%	9.26 wt.%
TA	1.19 wt.%	1.11 wt.%
RA	0.28 wt.%	0.30 wt.%

The WAC image (Figure 8a) shows that the tone is slightly darker and the density of the craters is lower within the range of Region MCD than Region N. The FA map (Figure 8b) indicates a relatively higher FA in Region MCD, and Table 3 shows that the average FA is 9.67 wt.% and it is about 0.41 wt.% higher than that of Region N. Figure 8c does not present a clear difference between Regions MCD and N, and the statistics present that the average TA of Region MCD is only 0.08 wt.% higher than Region N (Table 3). Then, though there is a faint difference within and beyond Region MCD, the deposits within the MCD are actually different from the surrounding regions.

Figure 8d and Table 3 indicate that the RA is largely similar within and surrounding Region MCD, indicating that the existence of the MCD is not related to the surface rocks.

Finally, the statistics of the TB performances hint at the reasonability of the extracted MCD. Table 4 presents the averages of the nTB during the daytime, nTB at night, and the four-band dTB of Region MCD and the nearby highlands (Region H). Here, the average nTB of Region MCD is greater during the daytime and lower at night than that of Region H; meanwhile, the average dTB of the former is apparently higher than the latter. Such TB behaviors coincide well with the numerical simulation with the theoretical models [20], indicating the existence of the MCD with mafic-rich materials is reasonable.

Table 4. The average nTB and dTB values of Region MCD and highland debris (H) in the Balmer–Kapteyn cryptomare region.

Channel	nTB at Daytime		nTB at Night		dTB (K)	
	MCD	H	MCD	H	MCD	H
3.0 GHz	1.003	0.998	0.998	0.998	3.64	2.41
7.8 GHz	1.006	0.999	0.998	0.999	8.64	6.74
19.35 GHz	1.005	0.996	0.996	1.000	21.60	18.19
37 GHz	1.004	0.993	0.990	1.001	48.39	43.06

Therefore, the MCD in the B-K cryptomare is reasonable. Additionally, the SVM method is an efficient way to objectively extract the MCD, which is used to study the other three cryptomare regions.

4.2. Extracting the MCD in Dewar, L-F, and S-S Cryptomare Regions

Considering the reasonability of the SVM method to extract the MCD from the B-K cryptomare region, we tried to extract the MCD from the Dewar, L-F, and S-S cryptomare regions with the same method, to verify whether the MCDs are widely distributed in the cryptomare regions or not.

The optimization of the training samples of the Dewar, L-F, and S-S cryptomare regions obtained based on the K-means algorithm are shown in Figure 9 (Column 1), where the purple, blue, and yellow colors respectively represent low-dTB materials (category 1), materials not clearly categorized (category 2), and the MCD (category 3). Here, category 1 shows a distinctly different TB performance compared to category 3; meanwhile, the TB behaviors of category 2 are not clearly different from category 3. Therefore, category 1 was

taken as non-MCD samples, while category 2 and category 3 were integrated as the MCD samples, which were then randomly sampled in a 20% proportion. Finally, 112, 500, and 500 training samples in corresponding cryptomare regions were selected. Such training samples optimization method can not only effectively avoid the output of small sample clustering regions, but can also maximize the accuracy of classification.

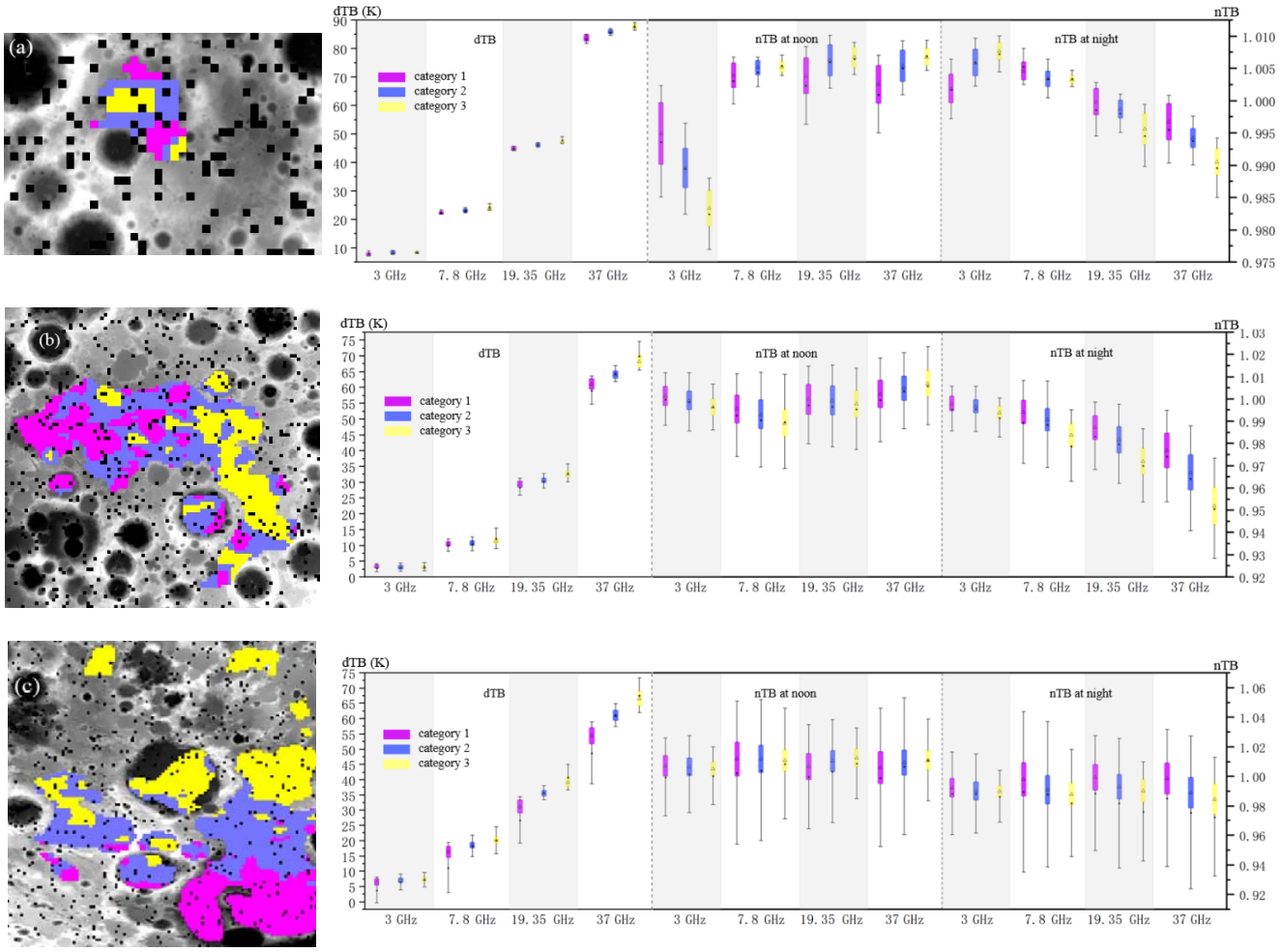

Figure 9. Column 1: The optimized training samples. The purple, blue, and yellow colors respectively represent low-dTB material (category 1), materials without a clear category (category 2), and the MCD (category 3), overlayed on the DEM map. The black points are randomly sampled in a 20% proportion. (**b**) Column 2: Numerical statistics of nTB and dTB characteristics of three categories. (**a**) Dewar, (**b**) Lomonosov–Fleming, and (**c**) Schiller–Schickard cryptomare regions.

Numerical statistics as shown in Figure 9 was conducted on the distribution characteristics of nTB and dTB of the optimized training samples, and the results showed that there were differences in the TB characteristics of the three categories as shown in Figure 9 (Column 2). From the upper limit and lower limit of dTB and nTB values, the dTB and nTB dynamic ranges of category 3 increase significantly with frequency increases. Therefore, the statistics of TB values indicate that the training samples are well optimized, which can better represent the corresponding category.

Using the RF algorithm, the importance of the band features can be calculated, as shown in Figure 10. To better represent the MCDs, the band features with the top 6 ranking in importance are extracted to operate the SVM method. The extracted band features for these three cryptomaria are shown in Table 2.

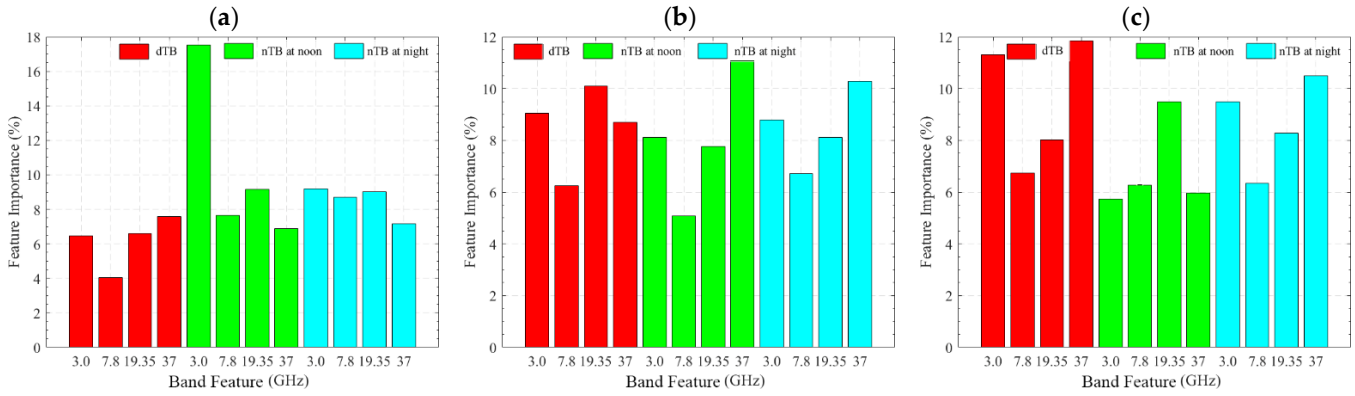

Figure 10. Importance of band features of nTB and dTB in the (**a**) Dewar, (**b**) Lomonosov–Fleming, and (**c**) Schiller–Schickard cryptomare regions.

Then, after optimizing the training samples and extracting the important band features, the MCDs in cryptomare regions are classified by using the SVM method.

Additionally, the RF algorithm is used to extract the proper dTB map as the background to postulate the distribution of the retrieved MCDs, as shown in Figure 11. To evaluate the reasonability of the new range of the region with MCDs, the extent of the cryptomare region interpreted by Whitten and Head [3], and the MCDs range presented by Tang et al. [20] are vectorized and overlaid on the extracted dTB map with the blue dotted line and green line, respectively (Figure 12).

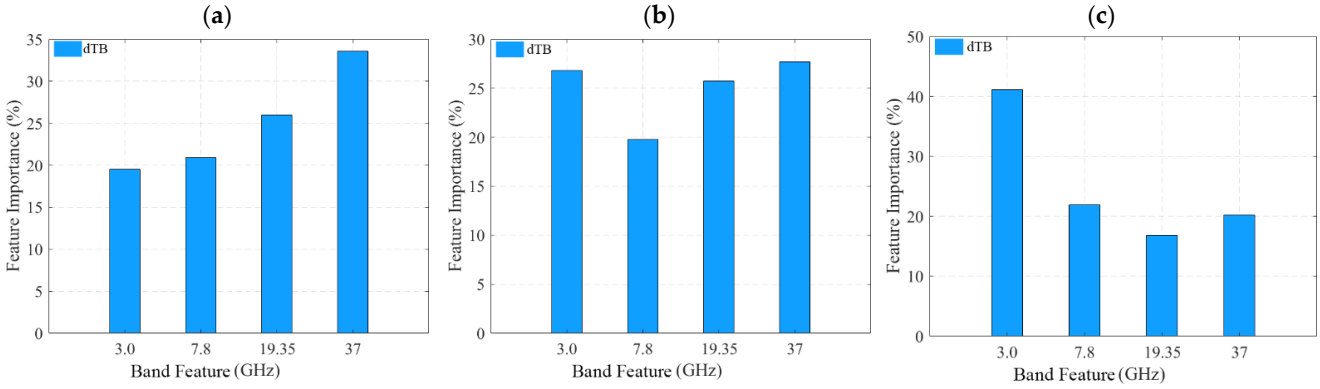

Figure 11. The importance of four-band dTB features in the (**a**) Dewar, (**b**) Lomonosov–Fleming, and (**c**) Schiller–Schickard cryptomare regions.

Similarly, these three cryptomare regions also prove the rationality of the existence of extracted MCDs through the WAC image, FA, TA, and RA of Region MCD and Region H, as well as the statistics of averages nTB and dTB values.

First, Figure 13 shows the WAC images, FA, TA, and RA maps; meanwhile, the average FA, TA, and RA with the range of Region MCD and Region N are counted, as shown in Table 5.

The WAC images (Figure 13) show that the tones are slightly darker and the density of the craters is lower within the range of Region MCD than Region N. The FA maps (Figure 13) and Table 5 indicate a relatively higher FA in Region MCD. Figure 13 (TA maps) and Table 5 do not present a clear difference between Regions MCD and N. Then, though there is a faint difference within and beyond Region MCD, the deposits within the MCD are actually different from the surrounding regions. Figure 13 and Table 5 indicate that the RA is largely similar within and surrounding Region MCD, indicating that the existence of the MCD is not related to the surface rocks.

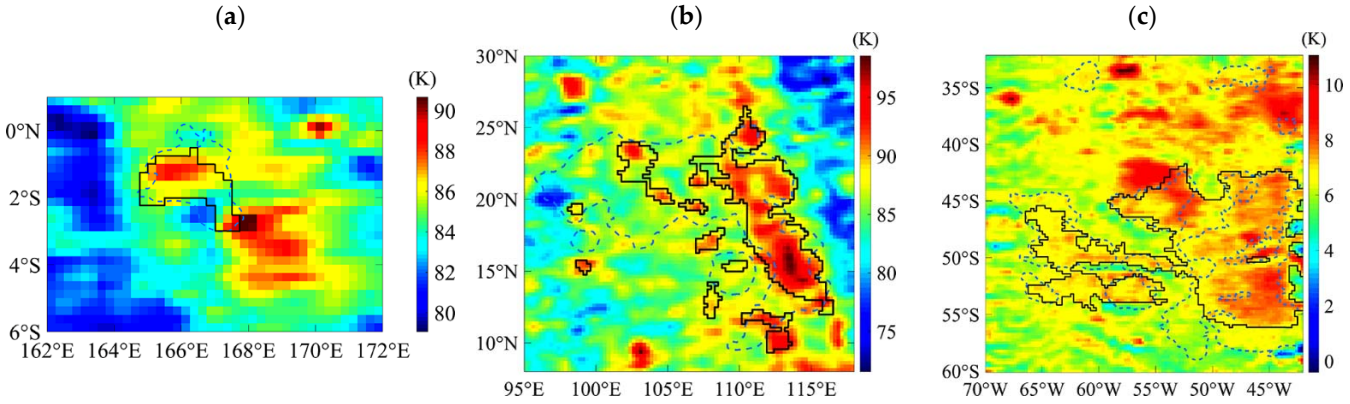

Figure 12. The distribution of the MCD (black line) in the (**a**) Dewar, (**b**) Lomonosov–Fleming, and (**c**) Schiller–Schickard cryptomare regions. The blue dotted lines are the extent of cryptomare regions interpreted by Whitten and Head [3].

Second, Table 6 presents the averages of the nTB during the daytime, nTB at night, and the four-band dTB of Region MCD and Region H. Here, the averages of the nTB in Region MCD in cryptomaria are greater in the daytime and lower at night than that of Region H; meanwhile, the averages of the dTB in the former are apparently higher than the latter. Such TB behaviors coincide well with the average nTB and dTB performances of the B-K cryptomare region, indicating the existence of the MCD with mafic-rich materials is reasonable and widely distributed.

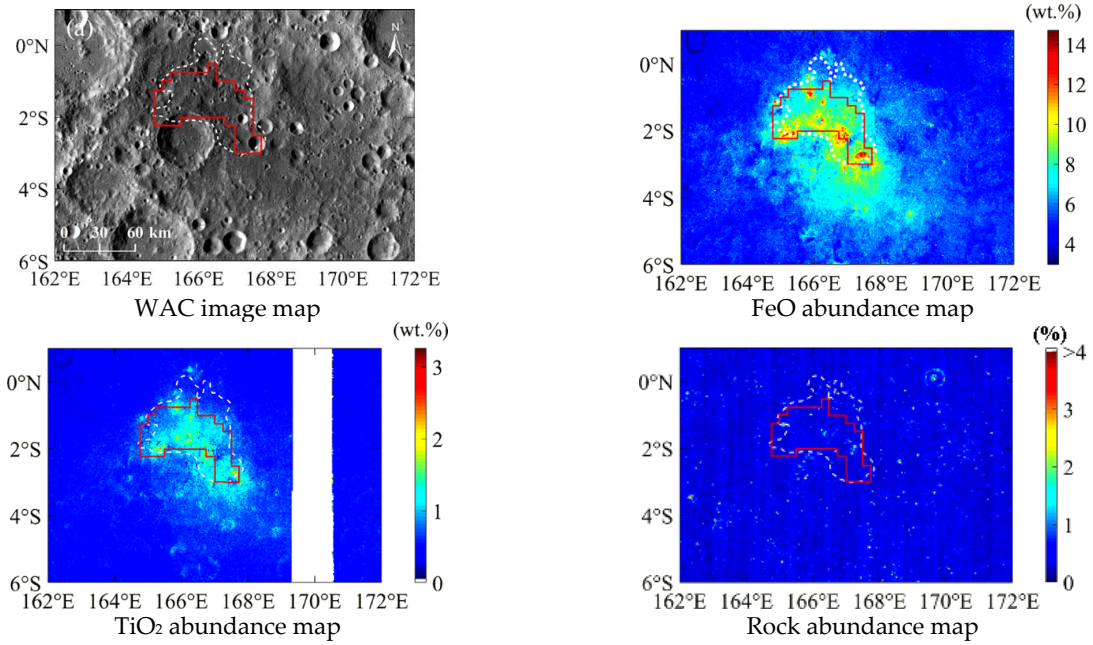

Figure 13. *Cont.*

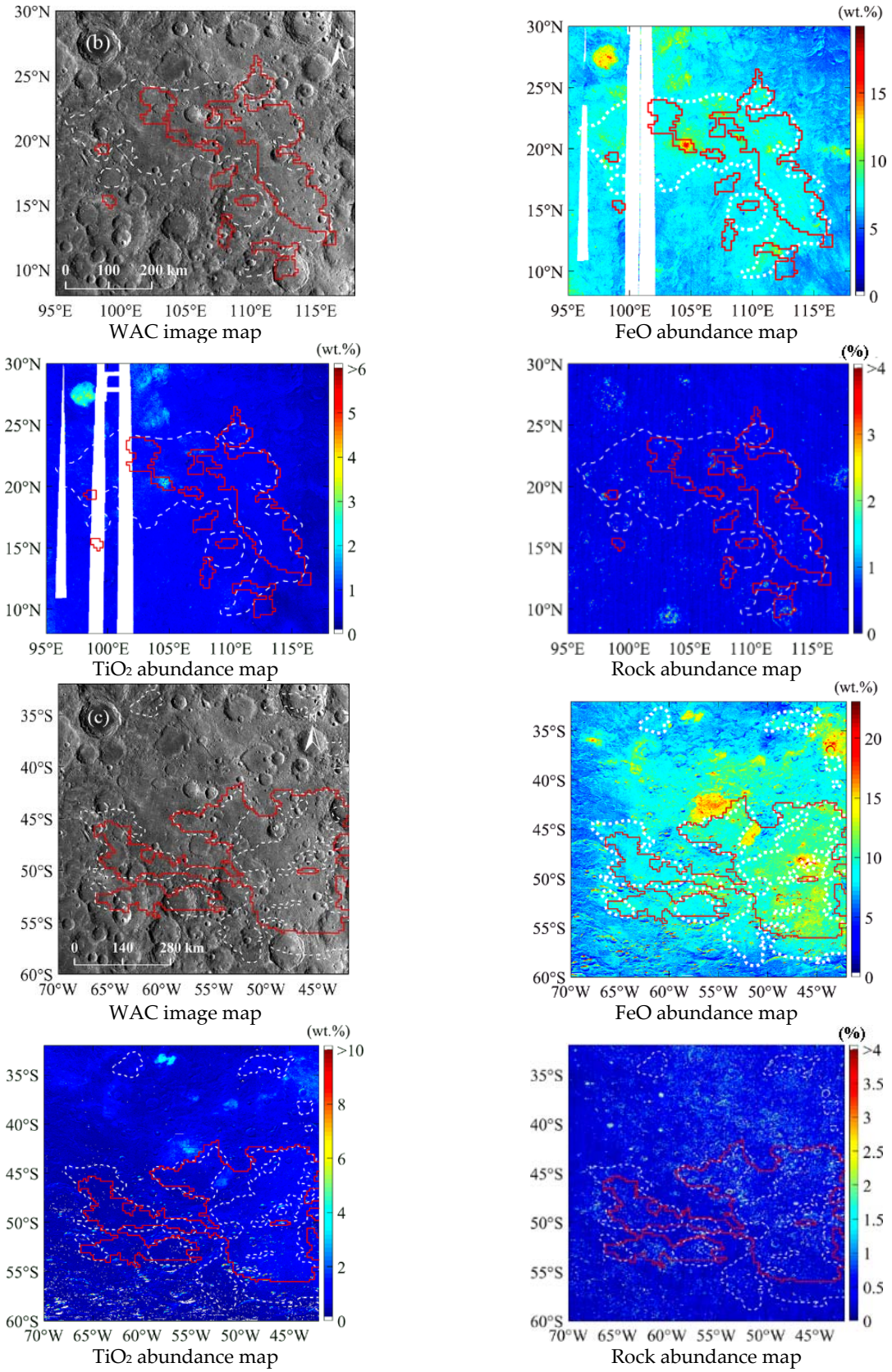

Figure 13. The maps in the (**a**) Dewar, (**b**) Lomonosov–Fleming, and (**c**) Schiller–Schickard regions. The red lines are the MCD extracted in this study. The white dotted lines are the cryptomare regions interpreted by Whitten and Head [3].

Table 5. The FeO abundance, TiO_2 abundance, and rock abundance of Region MCD and Region N in the Dewar, Lomonosov–Fleming, and Schiller–Schickard cryptomare regions.

Region	Compositions	Abundance	
		MCD	N
Dewar	FA	8.43 wt.%	8.22 wt.%
	TA	1.05 wt.%	0.99 wt.%
	RA	0.36 wt.%	0.33 wt.%
L-F	FA	7.48 wt.%	7.24 wt.%
	TA	0.66 wt.%	0.65 wt.%
	RA	0.33 wt.%	0.32 wt.%
S-S	FA	10.36 wt.%	9.82 wt.%
	TA	0.83 wt.%	0.75 wt.%
	RA	0.53 wt.%	0.52 wt.%

Table 6. The averages of the nTB and dTB values of Region MCD and highland debris (H) in the Dewar, Lomonosov–Fleming, and Schiller–Schickard cryptomare regions.

Region	Channel	nTB at Daytime		nTB at Night		dTB (K)	
		MCD	H	MCD	H	MCD	H
Dewar	3.0 GHz	1.005	1.002	1.003	1.003	8.27	8.23
	7.8 GHz	1.007	1.002	0.997	0.998	23.38	22.68
	19.35 GHz	1.006	1.000	0.993	0.993	46.57	44.68
	37 GHz	1.007	1.000	0.988	0.989	86.26	84.00
L-F	3.0 GHz	0.997	0.994	0.995	0.996	3.09	2.22
	7.8 GHz	0.990	0.984	0.985	0.989	11.18	9.11
	19.35 GHz	0.998	0.985	0.974	0.982	32.02	27.09
	37 GHz	1.006	0.988	0.955	0.968	67.13	59.93
S-S	3.0 GHz	1.007	1.007	0.990	0.996	7.28	5.97
	7.8 GHz	1.013	1.013	0.991	0.999	18.97	16.62
	19.35 GHz	1.012	1.005	0.993	0.997	36.24	31.67
	37 GHz	1.011	1.006	0.989	0.993	61.77	55.80

Figures 7 and 12 indicate that the existence of the MCD is about 3101.1 km^2 in Dewar, 59,078.3 km^2 in L-F, 173,097.3 km^2 in S-S, and 38,791.6 km^2 in B-K, which account for 64.9%, 52.3%, 76.4%, and 64% of the corresponding regions, as shown in Table 7. Therefore, the existence of the MCD in the cryptomare is extensive, that is, a considerable proportion of the cryptomare regions is covered by the deposits mixed by mare deposits with a certain fraction. Additionally, the existence of the mafic-rich deposits in the cryptomaria is extensive in the optical results, but from the aspect of the microwave, the extent of the MCD is rather limited. Thus, the usage of the MRM data presents a new view of the surface deposits in the cryptomare regions.

Table 7. The areas of the Dewar, Lomonosov–Fleming, Schiller–Schickard, and Balmer–Kapteyn cryptomare extents interpreted by Whitten and Head [3] (Region W) and the extracted MCD.

Region	W (km^2)	MCD (km^2)	Proportion (MCD/W)
Dewar	4780	3101.1	64.9%
L-F	113,000	59,078.3	52.3%
S-S	226,700	173,097.3	76.4%
B-K	60,600	38,791.6	64.0%

Moreover, Figures 7 and 12 indicate that the nTB and dTB values are not homogeneous within the MCD, hinting that the mixing fraction of the mare deposits is heterogeneous in the lateral direction. This presents a new way to further understand the formation mechanism and the surface evolution in the cryptomare, which deserves to be further studied.

5. Conclusions

MCD, defined as the highland debris mixed by the mare deposits with a high fraction, was first mentioned by Tang et al. [20] when studying the surface deposits in the B-K region, which is significantly important in understanding the thermal evolution of the cryptomare. In this study, to objectively extract the MCD with the CE-2 MRM data, the SVM method was adopted and the K-means algorithm was used to optimize the training samples and the RF algorithm was used to extract the band features. The main results are as follows.

First, the range of the MCD in the B-K cryptomare region is extracted objectively. The range is 63% larger compared to the results outlined via the 48-K-dTB isotherm by Tang et al. [20]. Moreover, by comparing with optical results, it is found that the new range is rational, which comprises the whole area with similar TB behaviors. This verifies that the SVM method is efficient to objectively extract the MCD.

Second, the ranges of the MCD in Dewar, L-F, and S-S cryptomaria are extracted with the SVM method. The comparison with datasets (WAC image, FA, TA, and RA) indicates the reasonability of the MCD. Moreover, the existence of the MCD occupies about 3101.1 km^2 in Dewar, 59,078.3 km^2 in L-F, and 173,097.3 km^2 in S-S cryptomaria. Thus, the usage of the MRM data presents a new view of the surface deposits in the cryptomare regions.

One more meaningful phenomenon is that the nTB and dTB values are not homogeneous within the MCD, which presents new content to improve understanding of the formation mechanism and the surface evolution in the cryptomare, which deserves to be further studied.

Author Contributions: Conceptualization, Z.M. and T.T.; methodology, Z.M. and Y.L.; software, Y.L. and Y.W.; validation, X.Z. and Z.C.; formal analysis, Z.M., A.G. and X.Z.; data curation, T.T.; writing—original draft preparation, T.T. and Z.M.; writing—review and editing, T.T., Z.M., Z.W., X.D., Y.Z., X.Z., Y.W., M.W. and Z.C.; visualization, T.T., X.D., Z.W. and Y.L.; supervision, Y.Z. and X.Z.; project administration, Z.M.; funding acquisition, Z.M. All authors have read and agreed to the published version of the manuscript.

Funding: This research was funded by the National Key R & D Program of China (No. 2021YFA0715104), the National Natural Science Foundation of China (No. 42071309), Natural Science Foundation of Jilin Province (No. 20220101159JC), the opening fund of State Key Laboratory of Lunar and Planetary Sciences (Macau University of Science and Technology), Macau FDCT grant number 119/2017/A3, and the Science and Technology Development Fund (FDCT) of Macau (Nos. 0059/2020/A2 and 014/2022/A1).

Data Availability Statement: In this study, the wide angle camera data are downloaded from (https://astrogeology.usgs.gov/search/map/Moon/LRO/LROC_WAC/Lunar_LRO_LROC-WAC_Mosaic_global_100m_June2013 (accessed on 5 March 2021)). The used CE-2 MRM data are available from Data Release and Information Service System of China's Lunar Exploration Program (https://moon.bao.ac.cn/ce5web/searchOrder_pdsData.search (accessed on 16 September 2020)). (FeO + TiO_2) abundances data are derived with the improved Lucey model [49] using the Clementine UV-VIS data, which are downloaded online (https://astrogeology.usgs.gov/search/map/Moon/Clementine/UVVIS/Lunar_Clementine_UVVIS_WarpMosaic_5Bands_200m (accessed on 8 September 2021)). The surface elevation data are downloaded from (https://pds-geosciences.wustl.edu/lro/lro-l-lola-3-rdr-v1/lrolol_1xxx/data/sldem2015/global/jp2, File sldem 2015 128 60s_60n_000_360.jp2 (accessed on 16 September 2020)). The rock abundance data are downloaded from https://pds-geosciences.wustl.edu/lro/lro-l-dlre-4-rdr-v1/lrodlr_1001/data/gdr_l3/cylindrical/jp2/(File dgdr_ra_avg_cyl_128_jp2.jp2 (accessed on 16 September 2021)).

Acknowledgments: The authors express their thanks to the people helping with this work, the providers of the data used in this article, and acknowledge the valuable suggestions from the peer reviewers.

Conflicts of Interest: The authors declare no conflict of interest.

References

1. Head, J.W.; Wilson, L. Lunar mare volcanism: Stratigraphy, eruption conditions, and the evolution of secondary crusts. *Geochim. Et Cosmochim. Acta* **1992**, *56*, 2155–2175. [CrossRef]
2. Antonenko, I.; Head, J.W.; Mustard, J.F.; Hawke, B.R. Criteria for the detection of lunar cryptomaria. *Earth Moon Planets* **1995**, *69*, 141–172. [CrossRef]
3. Whitten, J.L.; Head, J.W. Lunar cryptomaria: Mineralogy and composition of ancient volcanic deposits. *Planet. Space Sci.* **2015**, *106*, 67–81. [CrossRef]
4. Wang, X.; Qiu, D. Lunar Cryptomare: New Insights Into the Balmer-Kapteyn Region. *J. Geophys. Res. Planets* **2018**, *123*, 3238–3255. [CrossRef]
5. Bramson, A.M.; Carter, L.M.; Patterson, G.W.; Sori, M.M.; Morgan, G.A.; Jozwiak, L.M.; Nypaver, C.A.; Cahill, J.T.S. Burial Depths of Extensive Shallow Cryptomaria in the Lunar Schiller–Schickard Region. *Planet. Sci. J.* **2022**, *3*, 216. [CrossRef]
6. Schultz, P.H.; Spudis, P.D. *Evidence for Ancient Mare Volcanism*; Pergamon Press: Houston, TX, USA, 1979.
7. Schultz, P.H.; Spudis, P.D. Beginning and end of lunar mare volcanism. *Nature* **1983**, *302*, 233–236. [CrossRef]
8. Hawke, B.R.; Bell, J.F. Remote sensing studies of lunar dark-halo impact craters-Preliminary results and implications for early volcanism. In Proceedings of the Lunar and Planetary Science Conference Proceedings, Houston, TX, USA, 16–20 March 1981; pp. 665–678.
9. Hawke, B.R.; Gillis, J.J.; Giguere, T.A.; Blewett, D.T.; Lawrence, D.J.; Lucey, P.G.; Smith, G.A.; Spudis, P.D.; Taylor, G.J. Remote sensing and geologic studies of the Balmer-Kapteyn region of the Moon. *J. Geophys. Res. Planets* **2005**, *110*, E06004. [CrossRef]
10. Giguere, T.A.; Hawke, B.R.; Blewett, D.T.; Bussey, D.B.; Lucey, P.G.; Smith, G.A.; Spudis, P.D.; Taylor, G.J. Remote sensing studies of the Lomonosov-Fleming region of the Moon. *J. Geophys. Res. Planets* **2003**, *108*, 5118. [CrossRef]
11. Bell, J.F.; Hawke, B.R. Lunar dark-haloed impact craters: Origin and implications for early mare volcanism. *J. Geophys. Res. Solid Earth* **1984**, *89*, 6899–6910. [CrossRef]
12. Mustard, J.F.; Head, J.W.; Murchie, S.M.; Pieters, C.M.; Belton, M.S. Schickard cryptomare: Interaction between Orientale ejecta and pre-basin mare from spectral mixture analysis of Galileo SSI data. *Lunar Planet. Sci. Conf.* **1992**, *23*, 957.
13. Head, J.W.; Murchie, S.M.; Mustard, J.F.; Pieters, C.M.; Neukum, G.; McEwen, A.; Greeley, R.; Nagel, E.; Belton, M.J. Lunar impact basins: New data for the western limb and far side (Orientale and South Pole-Aitken basins) from the first Galileo flyby. *J. Geophys. Res. Planets* **1993**, *98*, 17149–17181. [CrossRef]
14. Hawke, B.R.; Spudis, P.D.; Clark, P.E. The origin of selected lunar geochemical anomalies: Implications for early volcanism and the formation of light plains. *Earth Moon Planets* **1985**, *32*, 257–273. [CrossRef]
15. Lawrence, D.J.; Feldman, W.C.; Elphic, R.C.; Little, R.C.; Prettyman, T.H.; Maurice, S.; Lucey, P.G.; Binder, A.B. Iron abundances on the lunar surface as measured by the Lunar Prospector gamma-ray and neutron spectrometers. *J. Geophys. Res. Planets* **2002**, *107*, 5130. [CrossRef]
16. Qiu, D.; Li, F.; Yan, J.; Wang, X.; Gao, W.; Deng, Q.; Guo, X. New view of the Balmer-Kapteyn region: Cryptomare distribution and formation. *Astron. Astrophys.* **2022**, *659*, A4. [CrossRef]
17. Zheng, Y.; Chan, K.; Tsang, K.; Zhu, Y.; Hu, G.; Blewett, D.T.; Neish, C. Analysis of Chang'E-2 brightness temperature data and production of high spatial resolution microwave maps of the Moon. *Icarus* **2019**, *319*, 627–644. [CrossRef]
18. Meng, Z.; Hu, S.; Wang, T.; Li, C.; Cai, Z.; Ping, J. Passive microwave probing mare basalts in mare imbrium using CE-2 CELMS data. *IEEE J. Sel. Top. Appl. Earth Obs. Remote Sens.* **2018**, *11*, 3097–3104. [CrossRef]
19. Meng, Z.; Lei, J.; Qian, Y.; Xiao, L.; Head, J.W.; Chen, S.; Cheng, W.; Shi, J.; Ping, J.; Kang, Z. Thermophysical Features of the Rümker Region in Northern Oceanus Procellarum: Insights from CE-2 CELMS Data. *Remote Sens.* **2020**, *12*, 3272. [CrossRef]

20. Tang, T.; Meng, Z.; Lian, Y.; Xiao, Z.; Ping, J.; Cai, Z.; Zhang, X.; Dong, X.; Zhang, Y. New Insights into Surface Deposits in the Balmer-Kapteyn Cryptomare Region Provided by Chang'E-2 Microwave Radiometer Data. *Remote Sens.* **2022**, *14*, 4556. [CrossRef]
21. Kodikara, G.R.; McHenry, L.J. Machine learning approaches for classifying lunar soils. *Icarus* **2020**, *345*, 113719. [CrossRef]
22. Chen, H.; Jing, N.; Wang, J.; Chen, Y.; Chen, L. A novel saliency detection method for lunar remote sensing images. *IEEE Geosci. Remote Sens. Lett.* **2013**, *11*, 24–28. [CrossRef]
23. Melgani, F.; Bruzzone, L. Classification of hyperspectral remote sensing images with support vector machines. *IEEE Trans. Geosci. Remote Sens.* **2004**, *42*, 1778–1790. [CrossRef]
24. Qian, Y.; Xiao, L.; Head, J.W. The Young Mare Basalts in Chang'E 5 Mission Landing Region, Northern Oceanus Procellarum. In Proceedings of the 51st Annual Lunar and Planetary Science Conference, Woodlands, TX, USA, 16–20 March 2020; p. 1459.
25. Lawrence, S.J.; Hawke, B.R.; Gillis-Davis, J.J.; Taylor, G.J.; Lawrence, D.J.; Cahill, J.T.; Hagerty, J.J.; Lucey, P.G.; Smith, G.A.; Keil, K. Composition and origin of the Dewar geochemical anomaly. *J. Geophys. Res. Planets* **2008**, *113*, E02001. [CrossRef]
26. Haines, E.L.; Etchegaray-Ramireez, M.I.; Metzger, A.E. Thorium concentrations in the lunar surface. II: Deconvolution modeling and its application to the regions of Aristarchus and Mare Smythii. *Lunar Sci. Conf.* **1978**, *9*, 2985–3013.
27. Hawke, B.R.; Spudis, P.D. Geochemical anomalies on the eastern limb and farside of the moon. In Proceedings of the Lunar Highlands Crust, Houston, TX, USA, 14–17 November 1979.
28. Clark, P.E.; Hawke, B.R. The lunar farside: The nature of highlands east of Mare Smythii. *Earth Moon Planets* **1991**, *53*, 93–107. [CrossRef]
29. Hawke, B.R.; Blewett, D.T.; Bussey, D.B.J.; Giguere, T.A.; Lawrence, D.J.; Lucey, P.G.; Smith, G.A.; Spudis, P.D.; Taylor, G.J. Geochemical anomalies in the lunar highlands. In Proceedings of the 34th Lunar and Planetary Science, League City, TX, USA, 17–21 March 2003.
30. Blewett, D.T.; Hawke, B.R.; Lucey, P.G.; Taylor, G.J.; Jaumann, R.; Spudis, P.D. Remote sensing and geologic studies of the Schiller-Schickard region of the Moon. *J. Geophys. Res. Planets* **1995**, *100*, 16959–16977. [CrossRef]
31. Mustard, J.F.; Head, J.W. Buried stratigraphic relationships along the southwestern shores of Oceanus Procellarum: Implications for early lunar volcanism. *J. Geophys. Res. Planets* **1996**, *101*, 18913–18925. [CrossRef]
32. Hareyama, M.; Ishihara, Y.; Demura, H.; Hirata, N.; Honda, C.; Kamata, S.; Karouji, Y.; Kimura, J.; Morota, T.; Nagaoka, H. Global classification of lunar reflectance spectra obtained by Kaguya (SELENE): Implication for hidden basaltic materials. *Icarus* **2019**, *321*, 407–425. [CrossRef]
33. Whitten, J.L.; Head, J.W. Lunar cryptomaria: Physical characteristics, distribution, and implications for ancient volcanism. *Icarus* **2015**, *247*, 150–171. [CrossRef]
34. Campbell, B.A.; Carter, L.M.; Hawke, B.R.; Campbell, D.B.; Ghent, R.R. Volcanic and impact deposits of the Moon's Aristarchus Plateau: A new view from Earth-based radar images. *Geology* **2008**, *36*, 135–138. [CrossRef]
35. Cai, Z.; Lan, T. Lunar brightness temperature model based on the microwave radiometer data of Chang'E-2. *IEEE Trans. Geosci. Remote Sens.* **2017**, *55*, 5944–5955. [CrossRef]
36. Meng, Z.; Chen, S.; Zheng, Y.; Cheng, W.; Hou, L. Mare Deposits Identification and Feature Analysis in Mare Australe Based on CECELMS Data. *J. Geophys. Res. Planets* **2020**, *125*, e2019JE006330. [CrossRef]
37. Zheng, Y.; Tsang, K.; Chan, K.; Zou, Y.; Zhang, F.; Ouyang, Z. First microwave map of the Moon with Chang'E-1 data: The role of local time in global imaging. *Icarus* **2012**, *219*, 194–210. [CrossRef]
38. Fang, T.; Fa, W. High frequency thermal emission from the lunar surface and near surface temperature of the Moon from Chang'E-2 microwave radiometer. *Icarus* **2014**, *232*, 34–53. [CrossRef]
39. Meng, Z.; Chen, S.; Wang, Y.; Wang, T.; Cai, Z.; Zhang, Y.; Zheng, Y.; Hu, S. Reevaluating Mare Moscoviense and its vicinity using Chang'E-2 microwave sounder data. *Remote Sens.* **2020**, *12*, 535. [CrossRef]
40. Liu, C.; Mei, L.; Meng, Z.; Wang, Y.; Zhu, K.; Cheng, W.; Cai, Z.; Ping, J.; Gusev, A. Special Thermophysical Features of Floor Materials in Mare Smythii Indicated by CE-2 CELMS Data. *IEEE J. Sel. Top. Appl. Earth Obs. Remote Sens.* **2021**, *14*, 8135–8143. [CrossRef]
41. Chan, K.; Tsang, K.; Kong, B.; Zheng, Y. Lunar regolith thermal behavior revealed by Chang'E-1 microwave brightness temperature data. *Earth Planet. Sci. Lett.* **2010**, *295*, 287–291. [CrossRef]
42. Matveev, Y.G.; Suchkin, G.L.; Troitskii, V.S. Change of Lunite Density with Depth in the Surface Layer. *Astron. Zhurnal* **1965**, *42*, 810.
43. Meng, Z.; Lei, J.; Xiao, Z.; Cao, W.; Cai, Z.; Cheng, W.; Feng, X.; Ping, J. Re-Evaluating Influence of Rocks on Microwave Thermal Emission of Lunar Regolith Using CE-2 MRM Data. *IEEE Trans.Rouse Craters A Wide Range Light Plain Geosci. Remote Sens.* **2022**, *60*, 1–12. [CrossRef]
44. Luo, M.; Ma, Y.; Zhang, H. A spatial constrained k-means approach to image segmentation. In Proceedings of the Fourth International Conference on Information, Communications and Signal Processing, 2003 and the Fourth Pacific Rim Conference on Multimedia. Proceedings of the 2003 Joint, Singapore, 15–18 December 2003; pp. 738–742.
45. Maheshwary, P.; Srivastav, N. Retrieving similar image using color moment feature detector and k-means clustering of remote sensing images. In Proceedings of the 2008 International Conference on Computer and Electrical Engineering, Dhaka, Bangladesh, 20–22 December 2008; pp. 821–824.
46. Breiman, L. Random forests. *Mach. Learn.* **2001**, *45*, 5–32. [CrossRef]

47. Huang, S.; Yin, J.; Zhu, H.; Cao, Z. Gaussian Attractive Force-Based Alternative Parametric Active Contour Model for 3D Lunar Crater Detection. In Proceedings of the IGARSS 2018–2018 IEEE International Geoscience and Remote Sensing Symposium, Valencia, Spain, 22–27 July 2018; pp. 7082–7085.
48. Jiang, C.; Shen, H.; Li, H.; Wang, Y. Optimal real-time lunar soft landing using random forest. *Chin. Space Sci. Technol.* **2018**, *38*, 8.
49. Lucey, P.G.; Blewett, D.T.; Taylor, G.J.; Hawke, B.R. Imaging of lunar surface maturity. *J. Geophys. Res. Planets* **2000**, *105*, 20377–20386. [CrossRef]